SSM/I Rain Retrievals within a Unified All-Weather Ocean Algorithm

FRANK J. WENTZ

Remote Sensing Systems, Santa Rosa, California

ROY W. SPENCER

Global Hydrology and Climate Center, NASA/Marshall Space Flight Center, Huntsville, Alabama

(Manuscript received 21 February 1996, in final form 4 April 1997)

ABSTRACT

A new method for the physical retrieval of rain rates from satellite microwave radiometers is presented. The method is part of a unified ocean parameter retrieval algorithm that is based on the fundamental principles of radiative transfer. The algorithm simultaneously finds near-surface wind speed W, columnar water vapor V, columnar cloud liquid water L, rain rate R, and effective radiating temperature T_U for the upwelling radiation. Comparisons with radiosondes demonstrate that the algorithm is able to retrieve water vapor when rain is present. For rain rates from 1 to 15 mm h^{-1}, the rms difference between the retrieved water vapor and the radiosonde value is 5 mm. A novel feature of the rain retrieval method is a beamfilling correction that is based upon the ratio of the retrieved liquid water absorption coefficients at 37 and 19 GHz. This spectral ratio decreases by about 40% when heavy and light rain coexist within the SSM/I footprint as compared to the case of uniform rain. This correction increases the rain rate when the spectral ratio is small. However, even with this beamfilling correction, tropical rainfall is still unrealistically low when the freezing level in the Tropics ($\sim$5 km) is used to specify the rain layer thickness. Realism is restored by reducing the assumed tropical rain-layer thickness to 3 km. This adjustment is probably compensating for two processes: 1) the existence of warm rain for which the rain layer does not extend to the freezing level and 2) very heavy rain for which the 19-GHz channels saturate. Global rain rates are produced for the 1991–94 period from two SSM/Is. The authors find that approximately 6% of the SSM/I observations detect measurable rain rates ($R > 0.2$ mm h^{-1}). The global rain maps show features that are, in general, similar to those reported in previously published rain climatologies. However, some differences that seem to be related to nonprecipitating cloud water are apparent.

1. Introduction

The accurate retrieval of oceanic rain rates from satellite microwave measurements has been an elusive goal since the concept was first proposed by Buettner (1963) and then demonstrated with satellite data by Wilheit et al. (1977). While the physical basis for these retrievals is sound, we believe that there are three significant assumptions inherent to these methods that make the measurement of tropical average rain rates to better than 10% problematic. These assumptions concern the specification of the following characteristics of a rain system: 1) the rain-layer thickness (often assumed to extend from the surface to the freezing level), 2) the relative amount of cloud water versus rain water, and 3) the varying rain intensities across the radiometer footprint (which is commonly called the ''beamfilling effect''). The observed brightness temperature (T_B) is strongly influenced by these three characteristics. Significant new information on these three issues will have to await the Tropical Rain Measurement Mission (TRMM; Simpson et al. 1988), scheduled to be launched in 1998. The combination of TRMM's microwave radiometer and rain radar will help to quantify the above three processes. In the meantime, while the new rain retrieval method described herein does not solve these problems, it does attempt to explicitly address them in a physically realistic way.

We present a unified, all-weather ocean algorithm that simultaneously finds the near-surface wind speed W (m s^{-1}), columnar water vapor V (mm), columnar cloud liquid water L (mm), rain rate R (mm h^{-1}), and effective radiating temperature T_U (K) for the upwelling radiation. This algorithm is a seamless integration of the Wentz (1997) no-rain algorithm and a newly developed rain algorithm. The algorithm is based on the fundamental principles of radiative transfer and explicitly shows the physical relationship between the inputs (T_B) and outputs (W, V, L, R, and T_U). The wind speed retrieval must be constrained to an a priori value for moderate to heavy rain, and T_U must be constrained by a statistical correlation for clear skies and light rain. The other retrieved

Corresponding author address: Frank J. Wentz, Remote Sensing Systems, Suite 220, 1101 College Ave., Santa Rosa, CA 95404.
E-mail: wentz@remss.com

parameters are unconstrained over the full range of weather conditions. Wentz (1997) discusses the algorithm's performance in the absence of rain, and herein we focus on the rain component of the algorithm.

A particular strength of the new method is its ability to ''orthogonalize'' the retrievals so that there is minimum cross talk between the retrieved parameters. With respect to estimating rainfall, it is important to remove the water vapor contribution to the observed brightness temperature. We will present results showing that the error in retrieved water vapor (as determined from radiosonde comparisons) is uncorrelated to the retrieved rain rate. Likewise, the influence of the radiating temperature T_U is separated from the liquid water signal by using the polarization information contained in the observations. Because the rain rates are retrieved only after all other significant influences on T_B are quantified, the various retrievals can be analyzed for climate relationships between them, with high confidence that there is a minimum of algorithm cross talk.

Conceptually, the rain retrieval involves the following steps. The physics of radiative transfer shows that there is a direct and unique relationship between brightness temperature and the atmospheric transmittance τ_L of liquid water. In view of this, the first step is to directly retrieve τ_L along with the other directly observable parameters W, V, and T_U. In the context of rainfall, τ_L is related to the columnar water in the rain cloud, and T_U provides information on the height from which the radiation is emanating and whether radiative backscattering by large ice particles is occurring (Spencer 1986). The retrieval of τ_L is done by solving a set of simultaneous brightness temperature equations. A basic premise in this retrieval is that the polarization signature of the T_B allows for the separation of the τ_L signal from the T_U signal. The T_B model is formulated such that the T_U parameter includes both radiative scattering effects and air temperature variability. In the next step, the spectral signature of the retrieved τ_L at 19 and at 37 GHz is used to estimate the beamfilling effect. A beamfilling correction is applied, and the mean atmospheric attenuation A_L for liquid water over the footprint is found. Mie scattering theory and an assumed relationship between cloud water and rain water are then used to convert the A_L to a columnar rain rate, which is defined as the vertically averaged rain rate times column height. Finally, the columnar rain rate is converted to a vertically averaged rain rate by dividing by an assumed rain column height that is a function of a sea surface temperature climatology. The final assumption is that the surface rain rate equals the vertically averaged rain rate. In this way, we explicitly handle the three rain cloud characteristics listed above.

The algorithm is developed and tested using the observations taken by the Special Sensor Microwave/Imager (SSM/I; Hollinger et al. 1987). The SSM/I is a scanning radiometer that operates at four frequencies: 19.35, 22.235, 37, and 85.5 GHz. It is flown by the Defense Meteorological Satellite Program (DMSP) on operational polar orbiting platforms. The results herein are based on SSM/I observations for the 4-yr period from 1991 to 1994. Observations from two satellites, *F10* and *F11*, are used. The *F10* observations cover the entire 4-yr period, while the *F11* observations begin in January 1992.

The algorithm described herein is being used to produce the NASA Pathfinder Data Set for Scanning Multichannel Microwave Radiometer and SSM/I. This dataset will be a 20-yr time series of geophysical parameters, which will be broadly distributed to the research community.

2. The no-rain algorithm

We begin by reviewing the no-rain algorithm described by Wentz (1997). Then section 3 shows how this algorithm is extended to include rain observations. In the absence of rain, there is a relatively simple and unique relationship between the ocean brightness temperature (T_B) measured by SSM/I and W, V, and L. As a consequence of this simple relationship, these parameters can be retrieved to a high degree of accuracy. The retrieval of (W, V, L) is accomplished by varying their values until the T_B model function matches the SSM/I observations. After a precision calibration to in situ observations, the rms retrieval accuracies for W, V, and L are 0.9 m s^{-1}, 1.2 mm, and 0.025 mm, respectively (Wentz 1997). We now give some details on the no-rain algorithm so that one can then see how it is extended to include rain.

The first step in the retrieval process is to average the SSM/I observations at 22 and 37 GHz down to the common spatial resolution of the 19-GHz antenna pattern, which is about 56 km. The retrievals of W, V, and L are done at this resolution, while the rain rate retrievals are done at the spatial resolution of the 37-GHz footprint, which is 32 km (see section 5). The no-rain algorithm then retrieves W, V, and L by solving the three model function equations

$$T_{A22V} = G_{VV}F_{22V}(W, V, L) + G_{VH}F_{22H}(W, V, L) + G_{VO}T_{BC}, \quad (1a)$$

$$T_{B37V} = F_{37V}(W, V, L), \quad (1b)$$

$$T_{B37H} = F_{37H}(W, V, L), \quad (1c)$$

where F is the model function. We have not included the wind direction term in the above equations because it is a small effect that is unimportant in the context of the rain algorithm. The SSM/I brightness temperatures at 37 GHz are denoted by T_{B37V} and T_{B37H} for vertical and horizontal polarization, respectively. The conversion of T_A to T_B requires dual-polarization observations, but only υ-pol observations are taken at 22 GHz. Thus at 22 GHz, we work in terms of the antenna temperature T_{A22V} rather than T_B. The term T_{BC} is the cold space

brightness temperature equaling 2.7 K. The G factors are the antenna pattern coefficients that account for antenna spillover and cross-polarization leakage (Wentz 1991). Equations (1) represent three quasilinear equations in three unknowns: W, V, and L. This system of equations is solved by Newton's method, as is explained in Wentz (1997).

3. Extending the algorithm to include rain

To create an all-weather algorithm, the no-rain algorithm is extended in the following ways.

1) The cloud water parameter L is replaced by the total transmittance of cloud and rain water at 37 GHz, τ_{L37}.
2) An additional parameter is added to the retrieval: total transmittance of cloud and rain water at 19 GHz, τ_{L19}.
3) When rain occurs, the wind speed retrieval is constrained to an a priori value.
4) When rain occurs, the effective air temperature T_U becomes a retrieved parameter.

The algorithm extensions are done such that the all-weather algorithm is identical to the no-rain algorithm when there is no rain and then smoothly transforms to a rain algorithm over the range from very light to moderate rain. Above about 2 mm h^{-1} the algorithm no longer retrieves wind speed. The first three modifications are discussed in this section, and the fourth modification involving the effective air temperature is discussed in section 5.

The first modification is to replace the argument L by the 37-GHz liquid water transmittance τ_{L37} for both cloud and rain water. In the no-rain algorithm, the cloud liquid water L enters the equation only through the transmittance. This dependence can be expressed as

$$\tau = \exp[-\sec\theta(A_O + A_V + A_L)] \tag{2}$$

$$A_L = \alpha_L[1 - 0.026(T_L - 283)]L, \tag{3}$$

where θ is the incidence angle, A_O and A_V are the atmospheric oxygen and water vapor absorptions, and A_L is the cloud liquid water absorption. Wentz (1997) gives expressions for A_O and A_V as functions of the effective air temperature and columnar water vapor. In the absence of rain, the radiative transfer through the cloud droplets, which are much smaller than the radiation wavelength, is governed by Rayleigh scattering, and the absorption is proportional to the columnar liquid water content L (mm) of the cloud (Goldstein 1951), as indicated by (3). The absorption has a small dependence on the temperature T_L of the cloud water.

The liquid water dependence in (2) can be equivalently expressed in terms of the liquid water transmittance τ_{LF},

$$\tau_F = \tau_{LF}^{\sec\theta(A_O + A_V)} \tag{4}$$

$$\tau_{LF} = \exp(-A_{LF}\sec\theta), \tag{5}$$

where τ_{LF} now replaces L as a retrievable parameter. The subscript F is introduced to denote the dependence on frequency. Often it is more convenient to work in terms of the absorption than the transmittance. Given the retrieved value for τ_{LF}, the absorption (before doing the beamfilling correction) is given by

$$A_{LF} = -\cos\theta \ln(\tau_{LF}). \tag{6}$$

When rain is present, the relationship between τ_{LF} and liquid water content is more complex, as discussed in section 7, and the simple Rayleigh expression is not valid. However, by parameterizing the T_B model in terms of τ_{LF} rather than L, we defer the problem of relating τ_{LF} to the liquid water content. In other words, we are dividing the rain retrieval problem into two steps. The first step involves separating the liquid water signal, expressed in terms of τ_{LF}, from the signal of the other parameters. Since T_B is nearly proportional to τ_{LF}^2 [see Eq. (21)], the beamfilling problem is not an issue when retrieving τ_{LF}. In the second step, a rain rate is inferred from τ_{LF}. It is only in the second step that one is required to make assumptions regarding the beam filling, the cloud/rain partitioning, and the rain column height.

The second modification is to introduce τ_{L19} as an additional parameter to be retrieved. For the no-rain algorithm, Rayleigh scattering gave a fixed relationship between the transmittances at 19, 22, and 37 GHz, and hence it was not necessary to separately retrieve τ_{L19}. However, when rain is present there is no fixed spectral relationship between the transmittances. Accordingly, we directly retrieve τ_{L19} by introducing a fourth equation into the retrieval process.

The third modification is to eliminate wind speed as a retrieved product when there is significant rain. The decrease in the atmospheric transmittance obscures the surface and degrades the ability to retrieve the wind speed. Furthermore, the T_B modeling error is larger for raining observations due to errors in specifying the effective air temperature, as is discussed in section 5. For moderate to heavy rain it is best to constrain the wind parameter to some specified a priori value. To do this, we use the SSM/I wind retrievals in adjacent, no-rain areas to specify W. If no such wind retrievals are available, we use a monthly, 1° latitude by 1° longitude wind climatology to specify W. This climatology is produced from 7 years of SSM/I observations.

These three modifications result in the following set of retrieval equations

$$T_{B19V} = F_{19V}(W, V, \tau_{L19}) \tag{7a}$$

$$T_{A22V} = G_{VV}F_{22V}(W, V, \tau_{L22}) + G_{VH}F_{22H}(W, V, \tau_{L22}) + G_{VO}T_{BC} \tag{7b}$$

$$T_{B37V} = F_{37V}(W, V, \tau_{L37}) \quad (7c)$$

$$T_{B37H} = F_{37H}(W, V, \tau_{L37}) - \Lambda(x)[F_{37H}(W_0, V, \tau_{L37}) - T_{B37H}]. \quad (7d)$$

The 22-GHz transmittance τ_{L22} is specified by an interpolation between τ_{L19} and τ_{L37}. The constraint on wind is accomplished by the $\Lambda(x)$ term, which is the weighting function given by

$$\Lambda(x) = \begin{cases} 0, & x < 0 \quad (8a) \\ 3x^2 - 2x^3, & 0 \le x \le 1 \quad (8b) \\ 1, & x > 1; \quad (8c) \end{cases}$$

$$x = (A_{L37} - 0.04)/0.11. \quad (9)$$

The weighting function $\Lambda(x)$ goes smoothly from 0 to 1 as its argument A_{L37} goes from 0.04 to 0.15. The lower bound of 0.04 represents the onset of rain and was found from an investigation of 38 northeast Pacific extratropical cyclones (Wentz 1990). The upper limit represents a rain rate of about 2 mm/h, depending on the rain column height and other factors. When $\Lambda(x) = 0$, the above equations have the same form as the no-rain equations (1). When $\Lambda(x) = 1$, Eq. (7d) simply becomes

$$F_{37H}(W, V, \tau_{L37}) = F_{37H}(W_0, V, \tau_{L37}), \quad (10)$$

where W_0 is the a priori wind speed. Equation (10) forces the wind retrieval to equal W_0. Thus A_{L37} plays the role of a blending parameter for joining the no-rain algorithm with the raining algorithm. As A_{L37} goes from 0.04 to 0.15, the algorithm smoothly transforms from the no rain algorithm to a rain algorithm. The set of equations (7) is solved in the same way as was discussed above for the no-rain algorithm. The equations are assumed to be stepwise linear in terms of the unknowns (W, V, τ_{L19}, τ_{L37}), and the equations are solved in an iterative manner. Typically about five iterations are needed to reach the 0.1-K convergence level.

4. Retrieval of water vapor in rain

Figure 1 shows the difference between the SSM/I retrieved water vapor and the value obtained from collocated radiosonde observations (RAOB). The difference is plotted versus rain rate. The quality control of the radiosonde data and the collocation with the SSM/I are discussed in Wentz (1997). There are a total of 35 108 SSM/I overpasses of radiosonde sites. For these overpasses, a total of 81 922 rain observations are found within a 112-km radius of the site. The solid curve shows the mean difference and the dashed curves show the ± 1 standard deviation of the difference. The rain rate is computed from the SSM/I observations, as described in this paper. The statistics are computed by first binning the observations into 0.5 mm/h rain-rate bins. For rain rates between 1 and 15 mm/h, the typical rms difference between the SSM/I and radiosonde vapor is 5 mm. In comparison, the rms difference for the no-rain

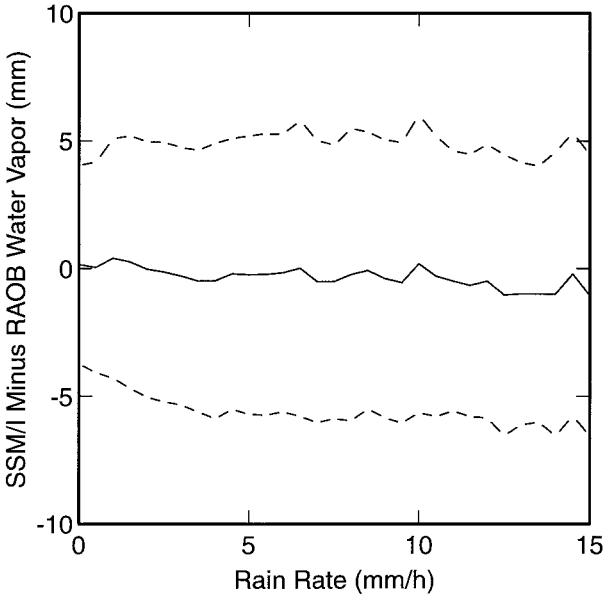

FIG. 1. A comparison of SSM/I and radiosonde columnar water vapor for rainy observations. The solid line is the mean difference, and the dashed lines show the one standard deviation envelope for the differences.

observations is 3.8 mm. The error analysis in Wentz (1997) indicates that the spatial and temporal sampling mismatch between the SSM/I 56-km footprint and the radiosonde point observation contributes about 3.7 mm to the total rms difference. Thus nearly all of the rms difference for the no-rain observations is due to the spatial–temporal mismatch. For the rain observations, about half of the rms difference is due to the spatial–temporal mismatch.

When we first compared the SSM/I and radiosonde water vapor, we found that for large A_{L19}, the SSM/I retrievals were biased low (high) relative to the radiosonde values for high (low) values of sea surface temperature T_S. In view of this, we apply the following ad hoc correction to the retrieved values of V in order to correct the observed systematic error:

$$V_{corr} = V_{ret} + 12(T_S - 283)(A_{L19} - 0.05)^{1.5}. \quad (11)$$

This correction has been applied to Fig. 1. We believe that this systematic error is due to radiative scattering and the degradation in the assumed relationship between the effective air temperature and water vapor, as is discussed in the next section.

We find that when A_{L19} exceeds about 0.3 (which corresponds to $R \sim 15$ mm/h, depending on rain column height), the atmosphere is too opaque and/or scattering is too strong to obtain a useful estimate of V. The procedure discussed in section 5 for obtaining τ_L when radiative scattering is significant requires that V be specified. Thus, for $A_{L19} > 0.3$, we use an a priori value for V based on the SSM/I vapor retrievals in adjacent, no-rain, and light-rain areas. If no adjacent retrievals are

available, we use a monthly, 1° latitude by 1° longitude vapor climatology to specify V. This climatology is produced from 7 years of SSM/I observations.

5. Effective air temperature and radiative scattering

Implicit in the T_B model function $F(W, V, \tau_L)$ is an assumed relationship for the effective air temperature T_U versus the retrieved columnar water vapor V and a climatological sea surface temperature T_S. The effective air temperatures, which we also call the effective radiating temperatures, for the upwelling and downwelling atmospheric radiation are defined as

$$T_U = T_{BU}/(1 - \tau) \tag{12a}$$

$$T_D = T_{BD}(1 - \tau), \tag{12b}$$

where T_{BU} and T_{BD} are the upwelling and downwelling atmospheric brightness temperatures and τ is the atmospheric transmittance. An analysis of 42 195 radiosonde observations shows that in the absence of rain T_U and T_D are well correlated with the V and T_S:

$$T_U = \Psi(V, T_S) \tag{13}$$

$$T_D = T_U - c_6 - c_7 V, \tag{14}$$

where the function $\Psi(V, T_S)$ and the coefficients c_6 and c_7 are given by Wentz (1997). At 19 and 37 GHz, T_U and T_D are very similar, with T_U being about 2 K colder.

When rain is present, the accuracy of $\Psi(V, T_S)$ degrades because 1) precipitation and associated convection alters the air temperature and 2) radiative scattering by large raindrops and ice particles reduces T_{BU} and T_{BD}. Since by definition T_U and T_D are proportional to T_{BU} and T_{BD}, they also decrease when scattering occurs. Fortunately, the radiosonde comparisons in the previous section show that the vapor retrieval error due to the degradation of $\Psi(V, T_S)$ is not large and can be partially corrected by the ad hoc adjustment (11). However, the error in τ_{L19} and τ_{L37} can be large if scattering effects are ignored. The rain algorithm accounts for scattering (and rain-induced variations in air temperature) by letting T_U become a retrieved parameter rather than being specified by $\Psi(V, T_S)$. Since V and W have already been found by the procedure described in section 3, the retrieval problem is reduced to two equations in two unknowns (i.e., T_U and τ_L):

$$T_{BV} = F_V(T_U, \tau_L) \tag{15a}$$

$$T_{BH} = F_H(T_U, \tau_L). \tag{15b}$$

There is a separate pair of equations for 19 and 37 GHz, and we have temporarily dropped the subscript denoting frequency. Two assumptions are required to solve these equations. First, T_U and T_D are assumed to be closely correlated so that T_D can be specified as a function of T_U according to (14). The second assumption is that T_U has the same value for vertical and horizontal polarization. In the absence of scattering, T_U is completely independent of polarization. For moderate to heavy rain, for which scattering is significant, SSM/I observations show that the saturation values for the v-pol and h-pol T_B observations are nearly the same (Spencer et al. 1989). Thus, the assumption of polarization independence seems reasonable.

Section 6 gives an example of how Eq. (15) are inverted to yield τ_L and T_U assuming a simplified T_B model. We denote the solution for T_U for the complete T_B model by the function

$$T_U = \xi(T_{BV}, T_{BH}). \tag{16}$$

We use this expression to specify the effective air temperature for the case of moderate to high rain rates. In order to blend this estimate of T_U with the no-rain estimate given by $\Psi(V, T_S)$, we use the expression:

$$T_U = [1 - \Lambda(u)]\Psi(V, T_S) + \Lambda(u)\xi(T_{BV}, T_{BH}), \tag{17}$$

$$u = (0.7 - \tau)/0.2, \tag{18}$$

and τ is the total transmittance τ of liquid water, water vapor, and oxygen. Equations (15a) and (17) are then combined to retrieve τ_L. When $\tau \geq 0.7$, then $T_U = \Psi(V, T_S)$, and the retrieved τ_L is identical to that found by the no-rain algorithm described in section 2. When the $\tau \leq 0.5$, the retrieved τ_L and T_U are based solely on the magnitude and polarization signature of the dual-polarization observations (either 19 or 37 GHz).

We define the depression ΔT_U in the effective temperature as

$$\Delta T_U = \xi(T_{BV}, T_{BH}) - \Psi(V, T_S), \tag{19}$$

which is a measure of the decrease in brightness temperature due to radiative scattering. In addition to radiative scattering, ΔT_U is also a measure of the decrease in the air temperature due to most of the radiation coming from the cold cloud tops. Figure 2 shows ΔT_U plotted versus τ for the time period from July to September 1992, as derived from the *F10* observations. For this time period, the SSM/I retrieval algorithm finds 7 859 295 rain-influenced footprints over the world's oceans. The curves are generated by binning these observations into $\Delta\tau = 0.01$ bins. The solid curves show the mean value for each bin, and the dashed curves show the ± 1 standard deviation for each bin. The depression in the effective temperature for the 37-GHz observations, which are most affected by scattering, is about twice that of the 19-GHz observations. For low values of τ, ΔT_U is about -10 K and -20 K for 19 and 37 GHz, respectively. For $\tau > 0.7$, the retrieved value of T_U given by $\xi(T_{BV}, T_{BH})$ for 19 GHz becomes noisy and unreliable.

The retrievals W, V, τ_L, and T_U are all done at the common spatial resolution of the 19-GHz channels, which is about 56 km. For the rain rate retrievals, we want as much spatial resolution as possible. In order to obtain a rain rate at the resolution of the 37-GHz foot-

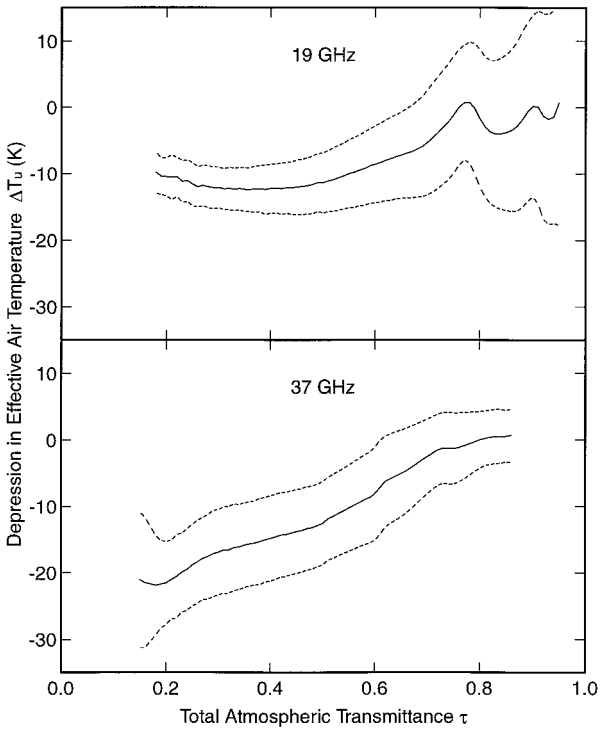

FIG. 2. The decrease in the effective air temperature due to radiative scattering and cold cloud-top temperatures.

print, we make the assumption that W and V are uniform over the 19-GHz footprint. The above equations are then used to find τ_{L37} and T_{U37} given the 37-GHz T_B at their original resolution of 32 km. In Fig. 2, the spatial resolution for the ΔT_U values is 56 km for 19 GHz and 32 km for 37 GHz.

The calculation of a beamfilling correction factor discussed in the next section requires both τ_{L19} and τ_{L37}. Thus to compute a rain rate at the 32-km resolution, a value of τ_{L19} at the spatial resolution of 32 km is required. We use the following expression to specify a high-resolution $\tau_{L19,\mathrm{HI}}$:

$$\ln(\tau_{L19,\mathrm{HI}}) = \ln(\tau_{L19})[\ln(\tau_{L37,\mathrm{HI}}/\ln(\tau_{L37})], \qquad (20)$$

where the subscript HI denotes the higher spatial resolution. Note that (20) is in terms of the absorption, that is, $\ln(\tau_L)$. The assumption behind Eq. (20) is that, even though the cloud and rain water may significantly vary over the footprint, the ratio of 19 to 37 GHz liquid water absorption is relatively constant. If this is true, then the observed spatial variation in τ_{L37} can be used as a scaling factor to compute τ_{L19} at the higher spatial resolution. In reality, this spectral ratio will have some interfootprint variability, and (20) will introduce some error into the rain retrieval. However, this error will tend to be unbiased and will tend to zero when doing spatial and temporal averages of rain rate.

6. The beamfilling effect

The terminology ''beamfilling effect'' refers to the nonlinear relationship between rain rate R and brightness temperature T_B that occurs when averaging over the radiometer footprint. To illustrate this effect, we use a relatively simple model for the brightness temperature:

$$T_B = T_E(\tau)(1 - \tau^2\rho), \qquad (21)$$

where $T_E(\tau)$ is the effective temperature of the combined ocean and atmosphere system, τ is the total transmittance through the atmosphere, and ρ is the reflectivity of the sea surface. The effective temperature is a function of τ. For $\tau = 1$, T_E equals the sea surface temperature T_S and, for $\tau = 0$, T_E equals the effective temperature T_U of the upwelling atmospheric radiation; T_E smoothly varies from T_S to T_U as τ goes from 1 to 0.

Despite its simplicity, Eq. (21) is actually a very good approximation to the complete T_B model function described in section 2 and provides considerable insight into the retrieval algorithm discussed in the previous sections. As discussed in section 5, to separate τ from the T_E signal requires dual-polarization observations, either at 19 or 37 GHz. Looking at the simple T_B model above, we see that the T_E term is easily eliminated, and the transmittance is given by

$$\tau^2 = \frac{T_{BV} - T_{BH}}{\rho_H T_{BV} - \rho_V T_{BH}}. \qquad (22)$$

Values for the wind speed and water vapor come from the procedure discussed in section 3. The wind speed and climatology sea surface temperature are used to specify ρ_V and ρ_H. The oxygen and water vapor components of τ^2 are factored out using Eq. (4), thereby obtaining just the liquid water transmittance τ_L^2. This method of using polarization information to separate the τ signal from the T_E signal is similar to that proposed by Petty (1994).

We see from (21) that for rain retrievals the basic observable is τ_L^2, which represents an average value over the SSM/I footprint. Equation (5) shows that the footprint average value of τ_L^2 is given by the integral

$$\tau_L^2 = \int e^{-2A'\sec\theta} P(A')\, dA', \qquad (23)$$

where the integral is over the probability density function $P(A')$ for the cloud and rain water absorption A' within the footprint. The desired retrieval is the mean absorption over the footprint, which is given by

$$A_L = \int A' P(A')\, dA'. \qquad (24)$$

Without any correction for the spatial averaging, the estimate of the absorption would be

$$\hat{A}_L = \frac{-\ln\tau_L}{\sec\theta}. \qquad (25)$$

Any variation of the absorption within the footprint will result in the estimate $\hat{A}_L$ being lower than the true mean value A_L. This systematic underestimation of the absorption is called the beamfilling effect.

If $P(A')$ is an exponential distribution of the form

$$P(A') = \frac{e^{-(A'/A_L)}}{A_L}, \tag{26}$$

then the integrals in (23) and (24) are easily evaluated, and one obtains the following relationship between A_L and $\hat{A}_L$:

$$A_L = \frac{e^{2\hat{A}_L\beta^2\sec\theta} - 1}{2\beta^2 \sec\theta}, \tag{27}$$

$$\beta = \frac{\Delta A_L}{A_L}. \tag{28}$$

Here ΔA_L is the rms variation of A' within the footprint and β is the normalized rms variation of A'. For an exponential distribution β equals unity. An expansion of statistical moments to the second order in $\hat{A}_L\beta^2$ shows that (27) is correct (to second order) for any distribution $P(A')$ having a mean A_L and an rms variation of ΔA_L. Thus if β is known, (27) can be used to correct the beamfilling effect. Here β is a normalized quantity that is related to the variability of liquid water in the footprint and hence is essentially independent of frequency.

In order to find β, we note that the ratio $\hat{A}_{L37}/\hat{A}_{L19}$ will be less than that predicted by Mie scattering theory when the beamfilling effect is significant. Thus comparing $\hat{A}_{L37}/\hat{A}_{L19}$ to the Mie absorption ratio provides the means to determine the beamfilling effect. The relationship between the Mie ratio and $\hat{A}_{L37}/\hat{A}_{L19}$ is given by the 37 to 19 GHz frequency ratio of Eq. (27):

$$\frac{A_{L37}}{A_{L19}} = \frac{e^{2\hat{A}_{L37}\beta^2\sec\theta} - 1}{e^{2\hat{A}_{L19}\beta^2\sec\theta} - 1}, \tag{29}$$

where the left-hand side is the Mie ratio given by Eq. (32) below. This ratio varies from 3.5 for light absorption values to 2.8 for heavy absorption. If the beamfilling effect is not significant, then $\hat{A}_{L37}/\hat{A}_{L19}$ will equal A_{L37}/A_{L19}. Thus when $\hat{A}_{L37}/\hat{A}_{L19} \geq A_{L37}/A_{L19}$, no beamfilling correction is done (i.e., β is set to 0). Otherwise (29) is inverted to find β as a function of the two ratios: $\hat{A}_{L37}/\hat{A}_{L19}$ and A_{L37}/A_{L19}. The inversion is readily done because the expression on the right-hand side of (29) increases monotonically with β. It equals $\hat{A}_{L37}/\hat{A}_{L19}$ when $\beta = 0$. Thus, the beamfilling correction consists of finding a value for β that when substituted into (29) yields the absorption ratio given by the Mie theory. Given β, the mean absorption for the footprint is then found (27).

The magnitude of the beamfilling correction is characterized in terms of the ratios $A_{L19}/\hat{A}_{L19}$ and $A_{L37}/\hat{A}_{L37}$, which are called the beamfilling correction factors (BCF). When $\hat{A}_{L37}/\hat{A}_{L19}$ is significantly less than A_{L37}/A_{L19}, large values for β and BCF are found. For example, when $\hat{A}_{L37}/\hat{A}_{L19} = 2$, the BCF is 1.4 and 2.0 for 19 and 37 GHz respectively. For even smaller values of $\hat{A}_{L37}/\hat{A}_{L19}$ the BCF increases exponentially, and we must impose the following limits. The maximum values of 3.4 and 6.4 are used for the 19-GHz and 37-GHz BCF, respectively, which corresponds to the exponent $2\hat{A}_{L37}\beta^2 \sec\theta$ in (29) reaching a value of 3.0. If the BCF exceeds the maximum, it is reset to the maximum. Another overall limit is placed on A_{L19} and A_{L37}. Neither value is allowed to exceed 1.2. These limits correspond to observations of heavy rain for which the 37 GHz and, to a lesser degree, the 19-GHz brightness temperatures have reached saturated levels. The effect of these limits is to place an upper hound on the retrieved rain rate. For the extreme case of A_{L19} reaching a value of 1.2, the retrieved rain rate will be about 25 mm/h (75 mm/h) for a rain column height of 3 km (1 km). We consider the 25 mm/h limit as an extreme upper bound on the algorithm's ability to retrieve rain. For such high rain rates, both the 19-GHz and 37-GHz observations have saturated, and the retrieval error can be very large.

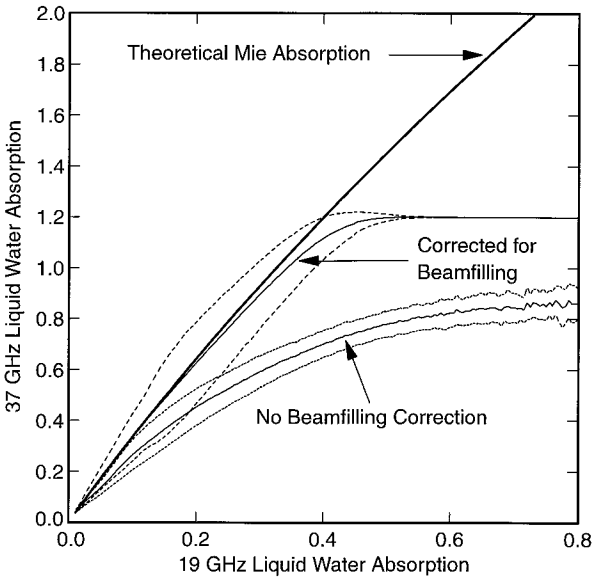

FIG. 3. The decrease in the observed 37 to 19 GHz absorption ratio due to the beam-filling effect.

Figure 3 shows the 37-GHz absorption plotted versus the 19-GHz absorption for the July–September 1992 period discussed in section 5. The bottom curve in Fig. 3 shows the retrieved absorptions $\hat{A}_{L37}$ versus $\hat{A}_{L19}$ before the beam-filling correction. The middle curve shows the absorptions A_{L37} versus A_{L19} after the beam filling correction, and the top curve shows the theoretical curve computed from Mie scattering computations. The curves are generated by binning the 7 859 295 observations into absorption bins having a width of 0.005. The solid curves show the mean value for each bin, and the dashed curves show the ± 1 standard deviation for each bin. The A_{L37} versus A_{L19} curve closely follows the theoretical curve up to values of $A_{L19} \approx 0.4$. Above this value, the

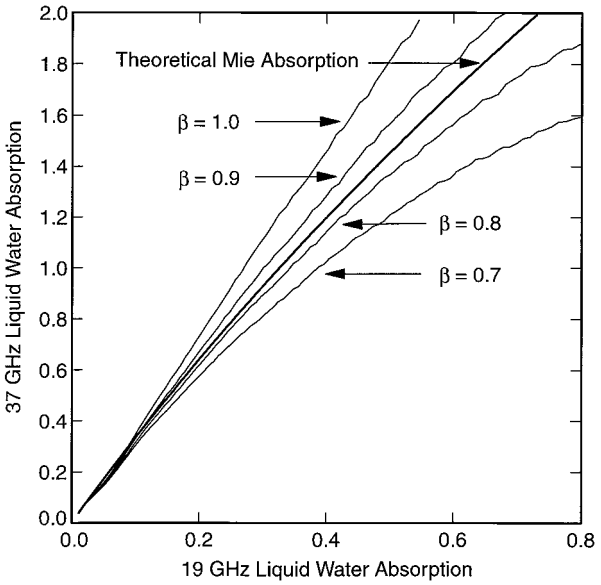

FIG. 4. Parametric curves showing the effect of the normalized spatial variability β of liquid water on the 37 to 19 GHz absorption ratio.

restriction that $A_{L37} \leq 1.2$ becomes important, and the curve asymptotically tends to the 1.2 value. For the high absorption bins, A_{L37} is a constant 1.2, and hence standard deviation envelope goes to zero.

Figure 4 shows the effect of the normalized rms variation β on the computation of A_{L37} and A_{L19}. For this figure, Eq. (27) is used to compute A_{L37} and A_{L19} from the retrieved values $\hat{A}_{L37}$ and $\hat{A}_{L19}$ using four different β values: 0.7, 0.8, 0.9, and 1.0. That is to say, rather than computing β for each observation, we use an average value. The theoretical Mie curve lies between the $\beta = 0.8$ and $\beta = 0.9$ curves. This indicates that, on the average, the beamfilling effect is characterized by a normalized rms variation $\beta \approx 0.85$, which is somewhat less than the $\beta = 1$ value given by an exponential probability density function for A_L.

7. Inferring rain rate from liquid water attenuation

In this section we describe how rain rate is inferred from the retrieved values of A_{L19} and A_{L37} once the beamfilling correction has been applied. The retrieval method discussed above results in A_L being directly related to the transmittance τ of the radiation from the sea surface upward through the atmosphere. Thus, more generally speaking, the retrieved A_L is an attenuation factor for the polarized sea surface signal traveling from the sea surface through the atmosphere. In the absence of scattering, the attenuation and absorption are equivalent and are given by

$$A_L = \int_0^H \kappa(h)\, dh, \qquad (30)$$

where the integral is over altitude h (km), $\kappa(h)$ (km^{-1}) is the Mie absorption coefficient, and H (km) is the height of the liquid water column. Radiative scattering from rain drops and ice modify the attenuation. For example, the attenuation for point-to-point microwave communication links is still given by (30), but $\kappa(h)$ is the Mie extinction coefficient, rather than absorption coefficient. However, the sea surface is an extended source, as opposed to a point source. For an extended source, the polarized surface signal traveling along the SSM/I viewing direction is scattered in other directions, while the surface signals traveling in other directions are scattered into the SSM/I viewing direction. These two effects tend to compensate, and using the extinction coefficient in (30) would overestimate the attenuation of the surface signal.

For moderate to heavy rain (R $\geq$ 10 mm/h), the 19-GHz (37-GHz) extinction coefficient is about 20% (60%) higher than the absorption coefficient. One distinguishing characteristic between the extinction and absorption coefficients is their spectral signature. For light to moderate rain (5 mm/h) the 37 to 19 GHz ratio for the extinction coefficient is 3.8 as compared to 3.0 for the absorption coefficient. Figure 3 shows that the spectral signature of the SSM/I retrieved $\hat{A}_{L37}/\hat{A}_{L19}$ is about 2 for light to moderate rain. Thus, a significantly larger beamfilling correction would be needed for the extinction coefficients as compared to the absorption coefficients. We decided to use the absorption coefficient to evaluate (30) because 1) its spectral signature is closer to the observed $\hat{A}_{L37}/\hat{A}_{L19}$ and 2) we expect that the attenuation of the polarized surface signal due to scattering will be small (i.e., the scattering into and out of the viewing direction will tend to cancel).

Fortunately, the choice of the attenuation coefficient does not have a large effect on the retrieved rain rate. The larger extinction coefficients would give a lower rain rate except for the fact that the beamfilling correction is larger for the extinction coefficients. These two factors tend to cancel each other, and, in general, the rain retrievals using the absorption coefficients are only about 10% higher than using the extinction coefficients. For example, if the best choice for κ in (30) is halfway between the absorption and the extinction coefficient, then our rain retrievals would be biased about 5% high.

The Mie absorption coefficient for a rain cloud is found by integrating the Mie absorption cross sections (Born and Wolf 1975) over the drop size distribution for the rain cloud, as described by Wilheit et al. (1977). The drop size distribution is partitioned into two parts: the nonprecipitating cloud water and the falling rain water. Then

$$\kappa = \int N_C(r)\sigma(r)\, dr + \int N_R(r)\sigma(r)\, dr, \qquad (31)$$

where r is the drop radius, $N_C(r)$ and $N_R(r)$ are the drop size distributions for cloud and rain water respectively,

and $\sigma(r)$ is the Mie absorption cross section. When r is much smaller than the radiation wavelength, which is the case for the cloud-water integral, $\sigma(r)$ is simply proportional to r^3, and hence the cloud integral is proportional to the total volume of cloud water per unit volume of atmosphere. Thus the vertically integrated cloud absorption given by (30) is proportional to the columnar cloud water L.

For the rain integral, the simple $\sigma(r) \propto r^3$ does not hold, and the absorption depends on the details of the drop size distribution. We use the Marshall and Palmer (1948) drop size distribution to specify $N_R(r)$. The Marshall–Palmer distribution is parameterized in terms of a nominal rain rate. Following the method described by Wilheit et al. (1977), we vary this nominal rain rate from 0.01 to 50 mm/h and compute the above rain absorption integral, denoted by κ_R, and the actual rain rate assuming the fall velocity given by Waldteufel (1973). We find that the κ_R versus rain rate relationship in the 19–37-GHz band is well approximated by a power law relationship, which is close to linear.

Combining (30) and (31) gives

$$A_{L19} = 0.059(1 - 0.026\Delta T)L + 0.0122(1 + 0.004\Delta T)HR^{1.06} \quad (32a)$$

$$A_{L37} = 0.208(1 - 0.026\Delta T)L + 0.0436(1 - 0.002\Delta T)HR^{0.95} \quad (32b)$$

$$\Delta T = T_L - 283, \quad (33)$$

where H is the height of the rain column, L is the columnar cloud water (mm), and T_L is the rain cloud temperature. The rain rate R (mm/h) is the rain rate averaged over the rain column given by

$$R = H^{-1} \int_0^H dh\, R(h), \quad (34)$$

where $R(h)$ is the rain profile. The difference between R and $R(0)$ is an additional source of error when comparing to in situ surface rain measurements. Evaporation under the rain cloud will tend to make R greater than $R(0)$, while a decrease in $R(h)$ at the top of the rain cloud will tend to make R less than $R(0)$. The rain cloud temperature is assumed to be the mean temperature between the surface and the freezing level,

$$T_L = (T_S + 273)/2, \quad (35)$$

where T_S is the climatology sea surface temperature.

Equation (32) reveals a fundamental problem in retrieving rain rate. Given just A_{L19} and A_{L37}, it is not possible to uniquely separate and retrieve L, R, and H. The spectral dependencies of the cloud water term and the rain rate term are nearly the same, as can be seen by the spectral ratio of the coefficients (0.208/0.059 = 3.5; 0.0436/0.0122 = 3.6). By doubling the rain rate R and halving the height H, one obtains about the same A_L. Thus to obtain an estimate for R, one must make a priori assumptions regarding L and H. Potentially, these assumptions can produce significant errors in the rain retrievals.

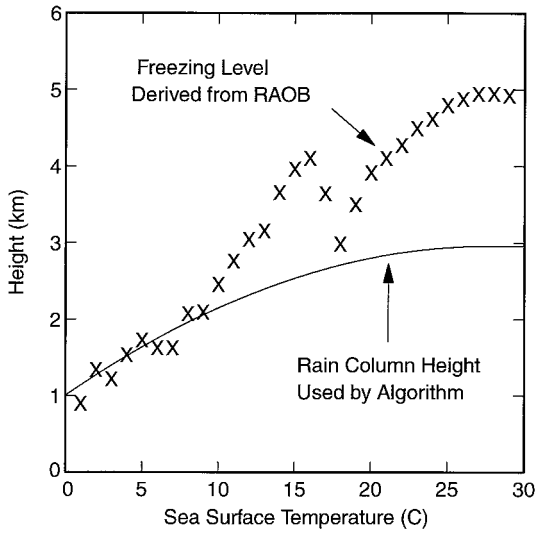

FIG. 5. The altitude of the atmospheric freezing level plotted vs the climatology sea surface temperature.

We know little of the statistics of cloud water versus rain rate in rain clouds. The data presented by Pruppacher and Klett (1980) indicate that heavy rain clouds can have values of L on the order of 1 to 2 mm. It seems reasonable to assume that, in general, L increases with R and then tend to level off at very high rain rates. Furthermore, an investigation of 38 northeast Pacific extratropical cyclones (Wentz 1990) indicates that when the SSM/I retrieval of L reaches a value of 0.18 mm, a drizzle or light rain is likely. The following expression incorporates the features of 1) rain beginning at L = 0.18 mm, 2) L increasing with R, and 3) the L versus R relationship leveling off at high R, with L reaching a maximum value between 1 and 2 mm,

$$L = 0.18\ (1 + \sqrt{HR}). \quad (36)$$

The specification of the rain column height H is based, in part, on the altitude H_F of the freezing level as derived from the radiosonde observations. The global radiosonde observations for the 1987–90 period collected by Wentz (1997) are used to find H_F as a function of the sea surface temperature T_S. Out of the total 42 195 radiosonde soundings, we only use the 9120 soundings for which the surface relative humidity is ≥90%. By restricting the dataset to high humidity cases, the results should be more indicative of rain observations. Figure 5 shows the height of the freezing level measured by the radiosondes versus the climatological sea surface temperature at the radiosonde site. For the stations at very high latitudes, the typical value of H_F is about 1 km. The midlatitude value of H_F ranges from 2 to 4 km, and in the Tropics H_F reaches a value of 5 km.

Equation (32) shows that the retrieved rain rate is

very nearly proportional to H^{-1}. Thus the proper specification of H is critical to obtaining good rain rate retrievals. In a preliminary analysis, we used the H_F values shown in Fig. 5 to specify H and found that the rain rates in the Tropics were about 40% lower in comparison to other climatologies (see section 8). We find that reducing to 3 km in the Tropics corrects the underestimation of rain relative to the climatologies. It is not unreasonable to expect that H is somewhat less than the freezing level because warm tropical rain does not extend up to the freezing level (Fletcher 1969). However, a reduction from 5 to 3 km seems extreme since warm rain is not that prevalent. Probably, this adjustment is compensating for some other deficiency in the algorithm, such as the algorithm's inability to accurately measure high rain rates. In any event, we let H be the one tuning parameter in the algorithm.

Outside the Tropics, we use H_F to specify H. The following simple regression, which is shown in Fig. 5, is derived so as to match H_F for low values of T_S and to reach a value of 3 km for high values of T_S:

$$H = 1 + 0.14(T_S - 273) - 0.0025(T_S - 273)^2, \qquad T_S < 301 \tag{37a}$$

$$H = 3, \qquad T_S \geq 301. \tag{37b}$$

Having specified H and the relationship between R and L, one can invert Eq. (32) and find a value for R given A_L. Note that, as a result of the beamfilling correction discussed in section 6, the retrieved values of A_{L19} and A_{L37} are not independent. Rather, they are computed such that their ratio is consistent with Eq. (32) above. For this reason, the same value for R is found from either A_{L19} or A_{L37}. The one exception is when A_{L37} exceeds the maximum value of 1.2. In this case, A_{L19} is used to compute the rain rate.

8. Rain-retrieval results

a. Probability density function of SSM/I rain rates

All results in this section are based on SSM/I observations for the 4-yr period from 1991 through 1994. Observations from two satellites, *F10* and *F11*, are used. The *F10* observations cover the entire 4-yr period, while the *F11* observations begin in January 1992. The top frame of Fig. 6 shows the probability density function (pdf) for the rain rates inferred from the two SSM/Is. The thick curve shows global results, and the thin curve shows tropical results (20°S–20°N). The computation of any rain pdf is very dependent on the temporal and spatial averaging. For the SSM/I, the temporal averaging is essentially instantaneous, and the spatial averaging has a resolution of about 32 km. A rain pdf computed from rain gauges looks very different than that shown in Fig. 6 because the spatial averaging is very different. The leftmost point on the pdf curves corresponds to the number of no-rain observations. A total of 85.9% of the SSM/I observations indicated no rain. An additional 8.3% of the observations indicated very light rain not exceeding 0.2 mm/h, and the remaining 5.8% of the observations indicate rain exceeding 0.2 mm/h. We consider the accuracy of the ''very light rain'' retrievals as questionable. Some or many of these observations may actually be heavy nonraining clouds. Note that the contribution of the very light rain observations to the total rainfall is very small (see below).

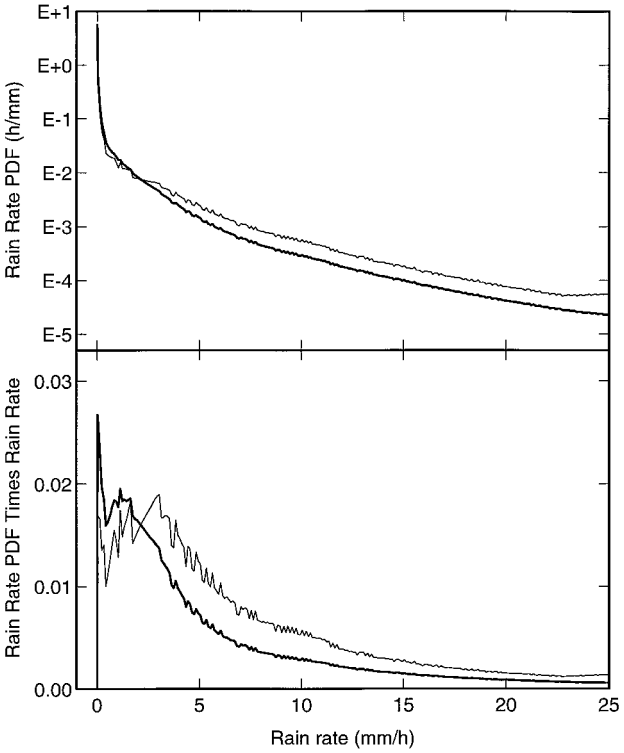

FIG. 6. The top frame shows the pdf for rain rate averaged over the SSM/I footprint. The bottom frame show the rain pdf times the rain rate. The thick curves show global results, and the thin curves show tropical results.

To determine the contribution of the various footprint-averaged rain rates to the overall rainfall amount, we multiply the rain pdf by the rain rate, as shown in the bottom frame in Fig. 6. In this case, the area under the curve equals the average oceanic rainfall, which is 0.12 mm/h (2.9 mm/day) globally and 0.16 mm/day (3.9 mm/day) in the Tropics. The questionable very light rain observations ($R < 0.2$ mm/h) only contribute 0.007 mm/h (0.17 mm/day) to this total. One-half of the total global oceanic rainfall occurs at footprint-averaged rates above (and below) about 3.5 mm/h. For rainfall in the Tropics, this midpoint value increases to 5.5 mm/h. Due to the large size of the footprint (32 km) over which the enveloped rainfall is averaged, this midpoint value is much lower than that obtained from rain gauges. Four-minute rain gauge statistics (Jones and Sims 1978) suggest that about half of tropical rainfall occurs at rates above about 20 mm/h. One possible interpretation of

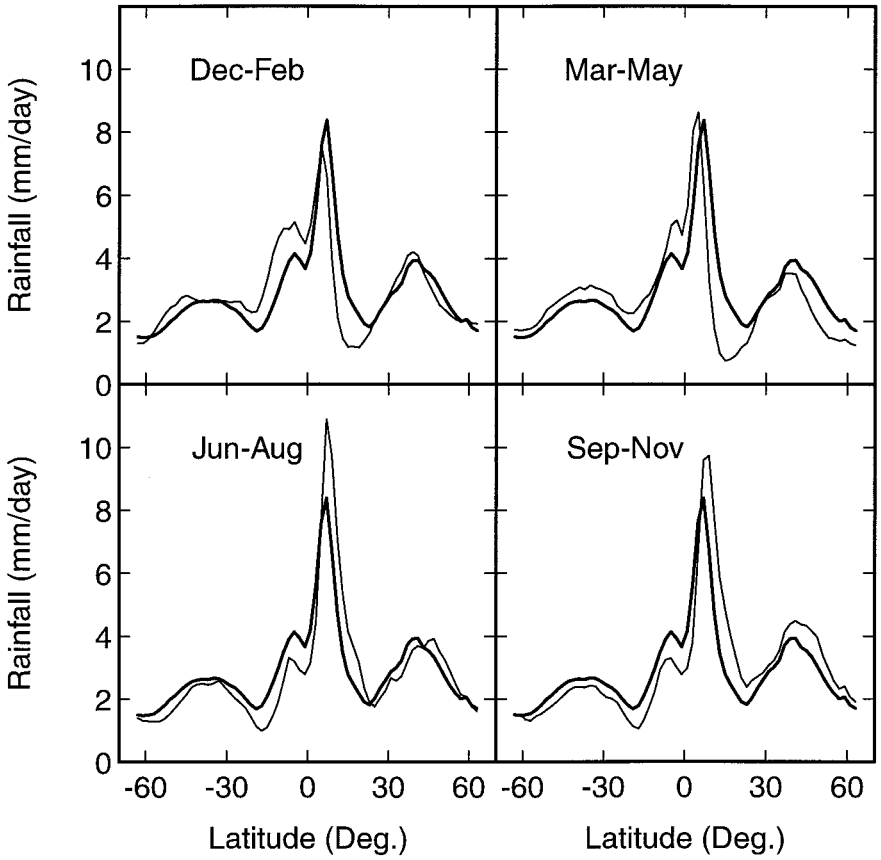

FIG. 7. The zonal average of rainfall over the ocean. The thick curve, which is repeated in each frame, is the annual average. The thin curve is the 3-month seasonal average.

this result is that, on the average when significant rain is being observed, only about one-quarter of the SSM/I footprint is actually covered by rain.

b. Global distribution of SSM/I rain rates

Figure 7 shows the seasonal and annual zonally averaged rainfall computed from the SSM/I observations for 1991–94. The meridional structures revealed by the SSM/I are similar to previously published climatologies. The maximum oceanic rainfall occurs at the equatorial latitudes associated with the strong convection in the intertropical convergence zone (ITCZ) for all seasons. This peak is quite narrow in meridional extent and varies from about 7 mm/day in the winter to a maximum 11 mm/day in the summer. The seasonal north–south migration of the ITCZ, which is in phase with the solar insolation, is also apparent in the figure. The extratropical rainfall is greater in the Northern Hemisphere than in the Southern Hemisphere for all seasons. Low precipitation rates ($\sim$1 mm/day) are observed in those zones of subsidence influenced by the large semipermanent anticylones.

Figure 8 shows color-coded global maps of the SSM/I annual and seasonal rainfall average over the four years from 1991 through 1994. The major features of the spatial distribution of the average annual rainfall are quite similar to those revealed in other satellite climatologies (see below). The largest annual rainfall amounts are seen to occur in the tropical Pacific, extending from South America to Papua New Guinea. Peaks of 15 mm/day occur throughout this band. Additional heavy rain associated with the Indian summer monsoons is apparent in the Bay of Bengal. The other major feature of the global rainfall maps is the extremely dry areas associated with the large semipermanent anticylones in the southeast Pacific and southeast Atlantic. These areas are essentially void of rain ($R < 0.3$ mm/day).

c. Comparison to other satellite climatologies

We now compare our rainfall estimates (hereafter WS) to two other emission-based rain climatologies: Spencer (1993, hereafter MSU), and Wilheit et al. (1991, hereafter WCC). The MSU rain rates are inferred from the 50.3-GHz T_B observations taken by the Microwave Sounding Unit (MSU). The WCC rain rates are inferred from the SSM/I T_B observations. The same period of record (1991–94) is used from these datasets. Figure 9 compares the three estimates of the annual zonally av-

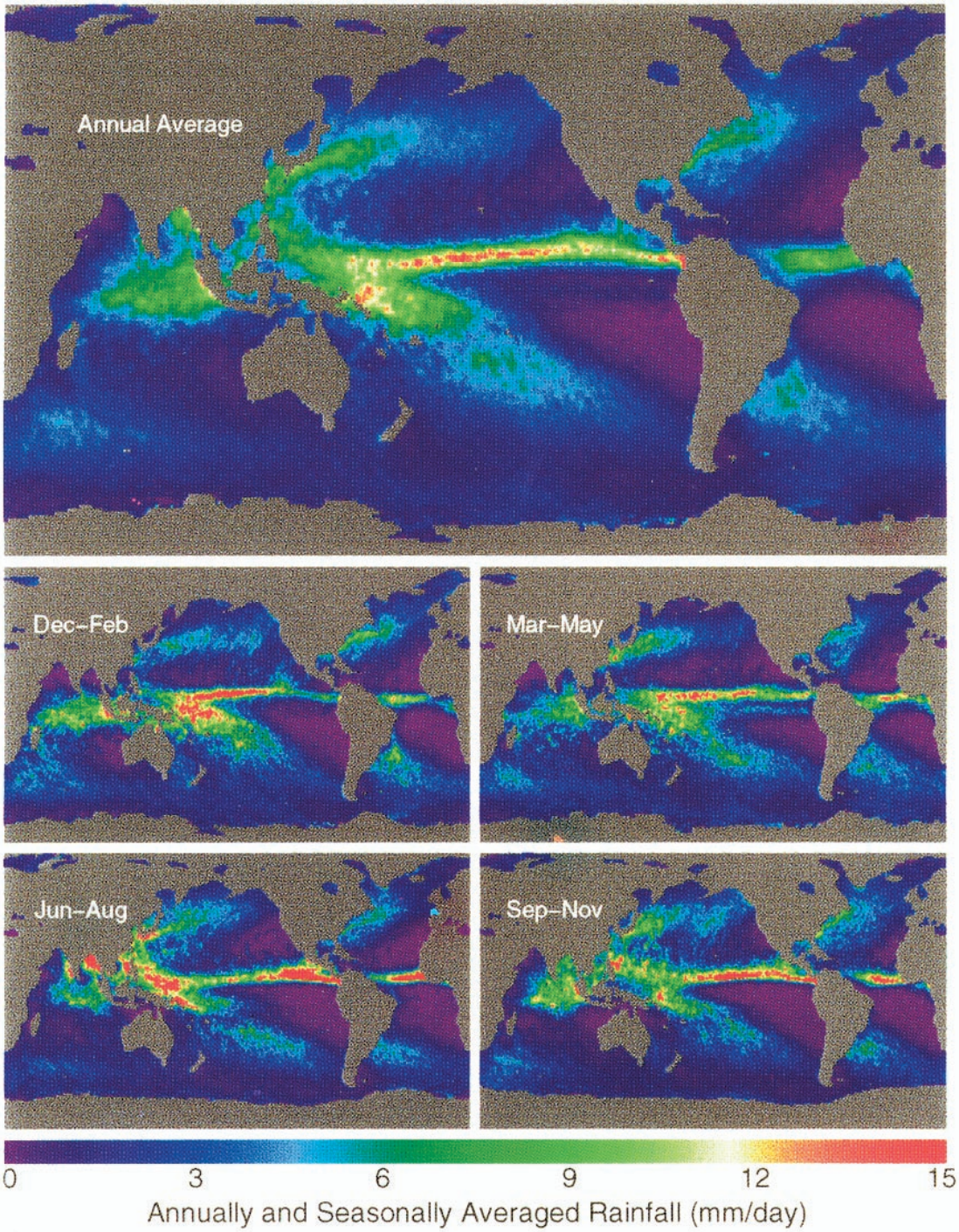

FIG. 8. Average rainfall for 1991–94 derived from SSM/I. The top map shows the annual rainfall, and the four smaller maps show the seasonal averages.

eraged rainfall. In general, the three rainfall estimates are similar, but there are some notable differences. We first note that above 50°N and below 55°S, the MSU rain data are contaminated by sea ice (see below). This explains the upturn at the two ends of the MSU curve in Fig. 9. In the ITCZ, the WS, MSU, and WCC reach maximum values of 8.1, 7.4, and 6.9 mm/day, respectively. This represents about a 15% difference between the highest estimate (WS) and the lowest estimate (WCC). In the extratropics storm track regions, the sit-

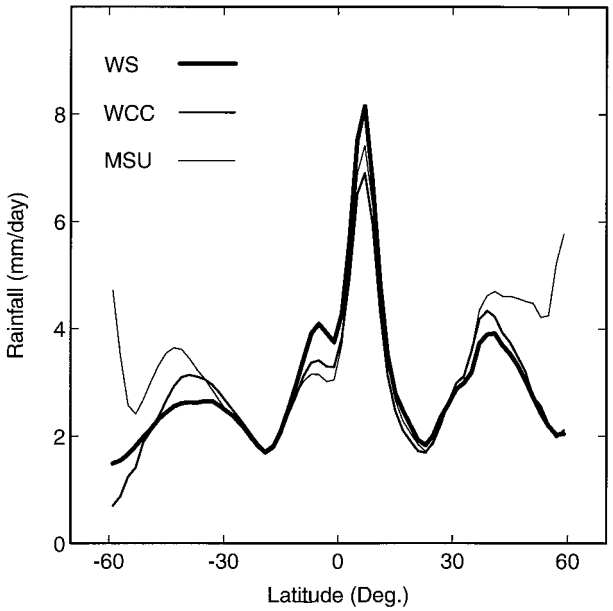

FIG. 9. A comparison of zonally averaged rain rates from three satellite climatologies: WS denotes our results, WCC denotes the Wilheit et al. (1991) results, and MSU denotes the Spencer (1993) results. The upturn at the two ends of the MSU curve is due to sea ice contamination.

uation changes. Here the WS rainfall is the lowest and MSU is the highest. Very close agreement is seen in the very dry areas associated with the semipermanent anticylones.

Figure 10 shows color-coded global maps of the MSU minus WS rainfall and the WCC minus WS rainfall. To compute these differences, the rainfall is averaged over the four years (1991–94) and then smoothed to a spatial resolution of about 300 km. The largest differences are seen between the MSU and WS. The MSU produces more rainfall in the downstream portions of the extratropical storm tracks and less rainfall over most portions of the Tropics, particularly in the tropical west Pacific. Comparisons of Fig. 10 to SSM/I retrievals of cloud water (not shown) suggest that the MSU–WS differences might be related to cloud water. Areas where the MSU–WS difference is significantly positive (negative) are moderately correlated with areas having a relatively high (low) cloud amount as compared to the rainfall. One example is the downstream portions of the extratropical storm tracks where there is significant cloud coverage but relatively little rain. In these regions the MSU rainfall is about 2 mm/day higher than WS. In contrast, along most of the ITCZ, the cloud content is relatively small compared to the heavy rain, the MSU rainfall is about 2–3 mm/day lower than WS. An interesting ocean area is seen just west of Central America and Columbia. The north (south) part of this area shows large negative (positive) MSU–WS differences. An analysis of SSM/I retrievals shows moderately heavy rain and relatively small cloud contents in the north and the reverse situation in the south, which is the same correlation as seen in the storm tracks and the ITCZ. The correct partitioning of cloud and rain water is a problem for both MSU and SSM/I. As pointed out by Spencer (1993), the hypersensitivity of the MSU 50.3-GHz channel to both cloud water and rainwater makes the MSU unable to distinguish between the two. We have somewhat more confidence in the SSM/I rainfall because the frequencies of 19.3 and 37 GHz are less sensitive to cloud water, and we have attempted to do a cloud versus rain partitioning. This confidence is bolstered by the fact that the cloud to rain ratio derived from SSM/I seems realistic. It is a minimum just off the east coasts of the continents where baroclinic wave activity is the strongest. Then this ratio increases eastward across the ocean basins, consistent with weaker wave activity.

The difference map between WS and WCC shows better agreement. The major difference is in tropical areas of heavy rain, where the WS is about 2 mm/day higher. In the extratropical storm tracks, the WCC is typically about 1 mm/day higher. In the dry areas, all three rain estimates (WS, MSU, and WCC) agree well. We find no obvious correlation between the WS–WCC difference and other parameters, except for the rainfall itself. When the rain is very heavy, WS tends to be higher than WCC.

Note that in the MSU–WS figure, the red areas in the Sea of Okhotsk, the Bering Sea, Hudson Bay, Labrador Sea, and off Antarctica are sea ice contamination in the MSU rain product. A very small amount of ice contamination is also seen in the WCC product just north of Japan.

9. Conclusions

A new method for the physical retrieval of rain rates and the effective radiating temperature T_U from the SSM/I has been presented. The method is part of a unified ocean parameter retrieval algorithm that also diagnoses total integrated water vapor, cloud water, and wind speed. We find that the water vapor retrievals maintain reasonably good accuracy when there is rain in the field of view. The rms difference between the SSM/I water vapor retrieval and radiosondes is about 5 mm for rain rates from 1 to 15 mm/h and the error is uncorrelated with the rain rate.

As expected, T_U exhibits a strong depression relative to the mean air temperature for moderate to heavy rain. This depression is due to 1) radiative scattering from large raindrops and ice and 2) the fact that most of the radiation is coming from the cold top part of the rain cloud. For the heaviest rain, the T_U depression is -10 K and -20 K for 19 and 37 GHz, respectively.

The spectral signature of the retrieved liquid water transmittance τ_L shows that the ratio of the 37-GHz to 19-GHz liquid water absorption is, on the average, about 40% lower than predicted by Mie theory for moderate

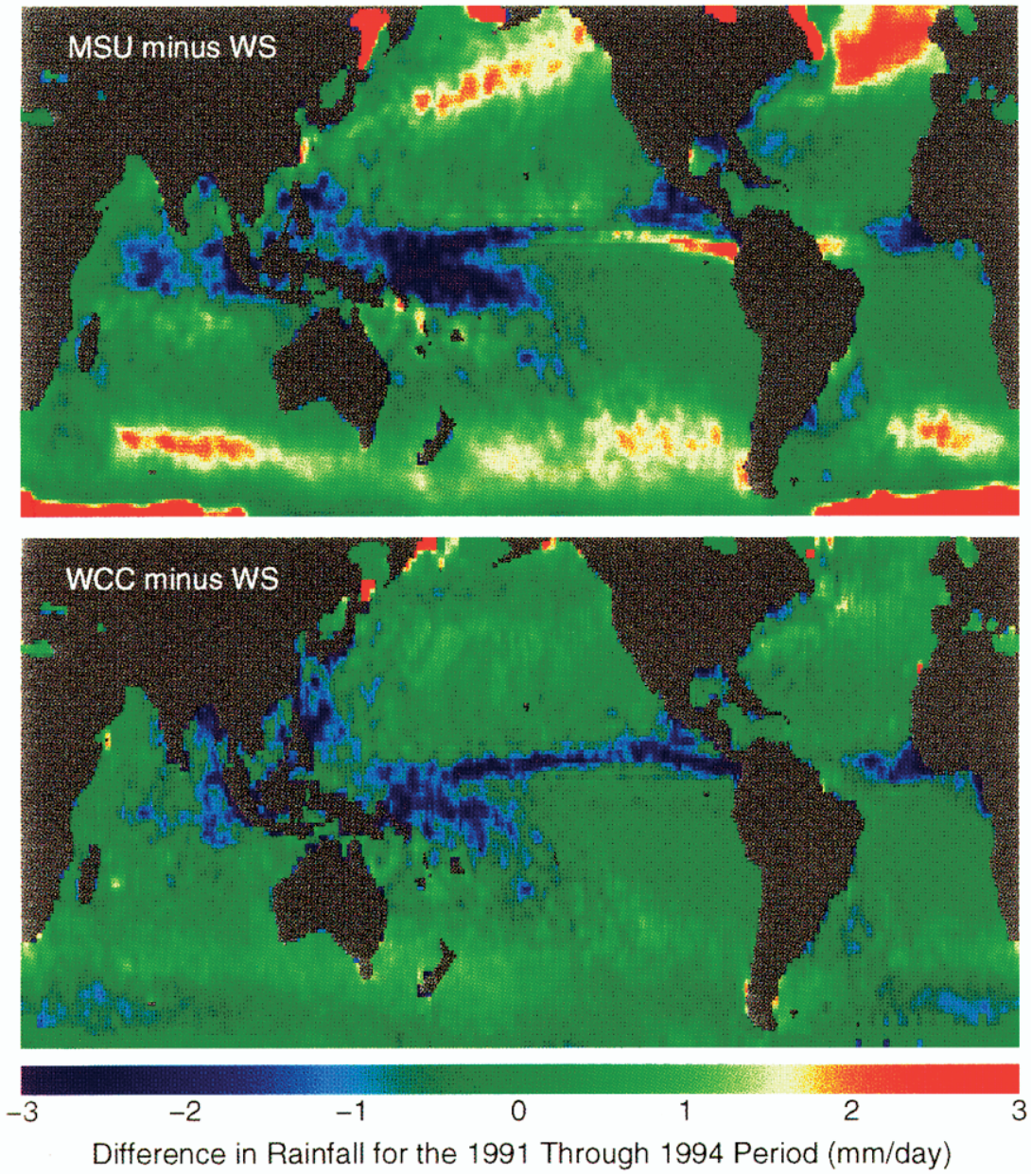

FIG. 10. A comparison of three satellite-derived rain maps. The top image shows the rainfall derived from the MSU (Spencer 1993) minus the SSM/I rainfall computed from the algorithm described herein (WS). The bottom image shows the rainfall produced by the Wilheit et al. (1991) algorithm (WCC) minus the WS rainfall.

to heavy rain. We attribute this difference to the beam-filling effect, which we parameterize in terms of the normalized rms variation β of the liquid water absorption A_L. To correct for this effect, the 37-GHz to 19-GHz liquid water absorptions are increased until the Mie ratio is realized. Globally, we find $\beta \approx 0.85$, which is somewhat less than that for an exponential pdf.

In the Tropics, we find using the freezing level, which is about 5 km, to specify H results in tropical rain rates that appear to be too low when compared with other rainfall climatologies. To correct the low bias, we use a value of $H \sim 3$ km in the Tropics. This adjustment is probably compensating for two processes: 1) the existence of warm rain for which the rain layer does not extend to the freezing level and 2) very heavy rain for which the 19-GHz channels saturate. Thus H plays the role of the one tuning parameter in the algorithm.

Global rain rates are produced for the 1991–94 period from two SSM/Is on board the *F10* and *F11* satellites. We find that on a global basis 6% of the SSM/I obser-

vations detect measurable rain rates of $R > 0.2$ mm/h. Globally, the average rainfall over the oceans is about 2.9 mm/day, and in the Tropics (20°N–20°S) it is 3.9 mm/day. Zonal averages and global maps of the retrieved rain rates show structures that are similar to those in previously published rain climatologies (Spencer 1993; Wilheit et al. 1991). However, some differences between the SSM/I and MSU rain rates are apparent and seem to be related to nonprecipitating cloud water.

Our rain retrieval technique could probably be improved by including the SSM/I 85-GHz channels. These channels are very sensitive to radiative scattering by ice and may provide the means to better identify areas of heavy rain exceeding 15 mm/h.

There still remains the problem of absolutely calibrating the rain algorithm. The lack of good quality in situ rain measurements over the oceans has been a major source of difficulty for all satellite-based rainfall estimation techniques, and it is still not clear how to best deal with the calibration problem. Hopefully future programs such as TRMM and the Precipitation Intercomparison Project will contribute to the better calibration of rainfall derived from satellites.

Acknowledgments. This research was supported by NASA's Oceans Program and EOS Program under Contracts NASW-4714 and NAS5-32594. We are thankful to the Defense Meteorological Satellite Program for making the SSM/I data available to the civilian community.

REFERENCES

Born, M., and E. Wolf, 1975: *Principles of Optics*. Pergamon Press, 182 pp.

Buettner, K. J. K., 1963: Rain localization from a weather satellite via centimeter waves (in German). *Naturwissenschaften,* **50,** 591.

Fletcher, N. H., 1969: *The Physics of Rainclouds.* Cambridge University Press, 390 pp.

Goldstein, H., 1951: Attenuation by condensed water. *Propagation of Short Radio Waves.* MIT Rad. Lab. Ser., Vol. 13, McGraw-Hill, 671–692.

Hollinger, J., R. Lo, G. Poe, R. Savage, and J. Pierce, 1987: Special Sensor Microwave/Imager user's guide. NRL Tech. Rep., Naval Research Laboratory, 120 pp. [Available from Space Sensing Branch, NRL, 4555 Overlook Ave. SW, Washington, DC 20375.]

Jones, D. M. A., and A. L. Sims, 1978: Climatology of instantaneous rainfall rates. *J. Appl. Meteor.,* **17,** 1135–1140.

Marshall, T. S., and W. Palmer, 1947: The distribution of raindrops with size. *J. Meteor.,* **5,** 165–166.

Petty, G. W., 1994: Physical retrievals of over-ocean rain rate from multichannel microwave imagery. Part I: Theoretical characteristics of normalized polarization and scattering indices. *Meteor. Atmos. Phys.,* **54,** 79–99.

Pruppacher, H. A., and J. D. Klett, 1980: *Microphysics of Clouds and Precipitation.* D. Reidel, 389.

Simpson, J., R. F. Adler, and G. R. North, 1988: A proposed Tropical Rainfall Measuring Mission (TRMM) satellite. *Bull. Amer. Meteor. Soc.,* **69,** 278–295.

Spencer, R. W., 1986: A satellite passive 37-GHz scattering-based method for measuring oceanic rain rates. *J. Climate Appl. Meteor.,* **25,** 754–766.

——, 1993: Global oceanic precipitation from the MSU during 1979–92 and comparisons to other climatologies. *J. Climate,* **6,** 1301–1326.

——, H. M. Goodman, and R. E. Hood, 1989: Precipitation retrieval over land and ocean with the SSM/I: Identification and characteristics of the scattering signal. *J. Atmos. Oceanic Technol.,* **6,** 254–273.

Waldteufel, P., 1973: Attenuation Des ondes hyperfrequences par la pluie: une mise au point. *Ann. Téléc.,* **28,** 255–272.

Wentz, F. J., 1990: SBIR Phase II Report: West coast storm forecasting with SSM/I. RSS Tech. Rep. 033190, 378 pp. [Available from Remote Sensing Systems, 1101 College Avenue, Suite 220, Santa Rosa, CA 95404.]

——, 1991: User's manual: SSM/I antenna temperature tapes, revision 1. RSS Tech. Rep. 120191, Remote Sensing Systems, 69 pp. [Available from Remote Sensing Systems, 1101 College Avenue, Suite 220, Santa Rosa, CA 95404.]

——, 1997: A well-calibrated ocean algorithm for SSM/I. *J. Geophys. Res.,* **102** (C4), 8703–8718.

Wilheit, T. T., A. T. C. Chang, M. S. V. Rao, E. B. Rodgers, and J. S. Theon, 1977: A satellite technique for quantitatively mapping rainfall over the oceans. *J. Appl. Meteor.,* **16,** 551–560.

——, ——, and L. S. Chiu, 1991: Retrieval of monthly rainfall indices from microwave radiometric measurements using probability distribution functions. *J. Atmos. Oceanic Technol.,* **8,** 118–136.